Whole-Body Radiation Dosimetry of ^{11}C-Carbonyl-URB694: A PET Tracer for Fatty Acid Amide Hydrolase

Isabelle Boileau[1–7], Peter M. Bloomfield[2], Pablo Rusjan[2,4], Romina Mizrahi[2,4,5,7], Asfandyar Mufti[7], Irina Vitcu[2], Stephen J. Kish[1–7], Sylvain Houle[2,4], Alan A. Wilson[2,4,5], and Junchao Tong[1–5]

[1]Addiction Imaging Research Group, Centre for Addiction and Mental Health, Toronto, Ontario, Canada; [2]Research Imaging Centre, Centre for Addiction and Mental Health, Toronto, Ontario, Canada; [3]Human Brain Laboratory, Centre for Addiction and Mental Health, Toronto, Ontario, Canada; [4]Campbell Family Mental Health Research Institute Centre for Addiction and Mental Health, Toronto, Ontario, Canada; [5]Department of Psychiatry, University of Toronto, Toronto, Ontario, Canada; [6]Department of Pharmacology, University of Toronto, Toronto, Ontario, Canada; and [7]Institute of Medical Science, Toronto, Ontario, Canada

^{11}C-carbonyl-URB694 (^{11}C-CURB) is a novel ^{11}C-labeled suicide irreversible radiotracer for PET developed as a surrogate measure of activity of the endocannabinoid metabolizing enzyme fatty acid amide hydrolase. The aim of the study was to investigate the whole-body biodistribution and estimate the radiation dosimetry from ^{11}C-CURB scans in humans. **Methods:** Six healthy volunteers (3 men and 3 women) completed a single whole-body scan (~120 min, 9 time frames) on a PET/CT scanner after administration of ^{11}C-CURB (~350 MBq and ~2 μg). Time–radioactivity curves were extracted in 11 manually delineated organs and corrected for injected activity, specific organ density, and volume to obtain normalized cumulated activities. OLINDA/EXM 1.1 was used to estimate standard internal dose exposure in each organ. The mean effective dose was calculated using the male and female models for the full sample and female-only sample, respectively. **Results:** ^{11}C-CURB was well tolerated in all subjects, with no radiotracer-related adverse event reported. The mean effective dose (±SD) was estimated to be 4.6 ± 0.3 μSv/MBq for all subjects and 5.2 ± 0.3 μSv/MBq for the female sample. Organs with the highest normalized cumulated activities (in h) were the liver (0.117), gallbladder wall (0.046), and small intestine (0.033), and organs with the highest dose exposure (in μGy/MBq) were the gallbladder wall (111 ± 60) > liver (21 ± 7), kidney (14 ± 3), and small intestine (12 ± 2). **Conclusion:** Organ radiation exposure for the irreversible fatty acid amide hydrolase enzyme probe ^{11}C-CURB is within the same range as other radiotracers labeled with ^{11}C, thus allowing for safe, serial PET scans in the same individuals.

Key Words: ^{11}C-CURB; fatty acid amide hydrolase; positron emission tomography; dosimetry; endocannabinoid system

J Nucl Med 2014; 55:1993–1997
DOI: 10.2967/jnumed.114.146464

Fatty acid amide hydrolase (FAAH) is a serine hydrolase catabolic enzyme that breaks down the ubiquitous lipophilic signaling molecule anandamide (*N*-arachidonoyl-ethanolamine), an endocannabinoid neurotransmitter, as well as other bioactive fatty acid amides, for example, oleoylethanolamide and palmitoylethanolamide (*1*). It is abundantly expressed throughout the body (with highest presence in the liver) and in the brain (*2–4*). It tightly regulates anandamide activity at the prevalent G-protein–coupled brain CB1 receptor; peripheral CB2 cannabinoid receptors; and transient receptor potential vanilloid type 1, a nonselective cation channel that belongs to the transient receptor potential channel family (*5*). Accordingly, FAAH is believed to indirectly modulate important primary functions and behaviors including energy homeostasis, nociception, inflammation, neuroendocrine response, reproduction, locomotion, mood, and cognition (*6*). Given the presumed role of this enzyme in a variety of human neuropsychiatric and neurodegenerative disorders (including anxiety, depression, eating disorders, addictions, fibromyalgia, schizophrenia, Huntington disease, and Parkinson disease), FAAH inhibitors have been avidly pursued as therapeutic targets and several attempts have been made to develop a PET radiotracer to measure FAAH activity in vivo.

We recently reported the radiolabeling of URB694 (6-hydroxy-[1,10-biphenyl]-3-yl cyclohexylcarbamate), a close analog of the prototypical carbamate FAAH inhibitor URB597, using a novel ^{11}C-CO_2 fixation technique yielding ^{11}C-carbonyl-URB694—that is, ^{11}C-CURB (*7*). The radiotracer ^{11}C-CURB is a highly specific and potent suicide irreversible inhibitor of FAAH. Our studies show that regional brain uptake of ^{11}C-CURB corresponds with the known distribution of FAAH in rat brain; specifically, greater uptake is noted in the cerebral cortex, with lowest uptake in the FAAH-poor hypothalamus region.

The potential of ^{11}C-CURB as a radiotracer to image FAAH in humans has already been shown (*8*); however, the radiation dosimetry estimates for those studies had been obtained by extrapolation from rat studies (*7*). This study provides updated dose estimates based on biodistribution data obtained directly in humans.

MATERIALS AND METHODS

Radiosynthesis of ^{11}C-CURB

The radiosynthesis of ^{11}C-CURB has been described earlier (*8*). The method uses a novel 1-pot automated ^{11}C-CO_2 fixation reaction to form carbonyl-^{11}C-*O*-arylcarbamates at high specific activities and in radiochemical purities exceeding 97%. The purified radiotracer was formulated for injection as a sterile, pyrogen-free solution in saline containing 0.5% polysorbate80 (Sigma-Aldrich).

Received Jul. 31, 2014; revision accepted Oct. 16, 2014.
For correspondence or reprints contact: Isabelle Boileau, Centre for Addiction and Mental Health, 250 College St., Toronto, ON, Canada M5T 1R8.
E-mail: isabelle.boileau@CAMH.ca
Published online Nov. 20, 2014.

Subjects

All procedures were approved by the Centre for Addiction and Mental Health Research Ethics Board and complied with ethical standards of the 1975 Helsinki Declaration. Subjects were recruited from the local community in Toronto, Canada, through advertisements. Six healthy volunteers (3 men and 3 women; weight, 67 ± 6 kg; height, 167 ± 4 cm; age, 36.5 ± 12 y; body mass index < 30) provided written informed consent to participate after all procedures were fully explained. All subjects were free of medical and Axis I psychiatric conditions (as per detailed medical history, Structured Clinical Interview for DSM-IV Axis I Disorders (*9*), electrocardiogram, urinalysis including drug screening, and comprehensive blood chemistry screen). Women of child-bearing potential were screened for pregnancy (exclusion criterion).

PET Acquisition and Image Reconstruction

Studies were performed using a whole-body PET/CT scanner (Biograph HiRez XVI; Siemens Molecular Imaging) (*10*). The CT component of the system is a 16-slice scanner and is used for positioning subjects and acquiring a minimal-dose CT scan, from which the attenuation correction for the PET emission scan is calculated. The in-plane resolution of the PET scanner is approximately 4.6 mm in full width at half maximum (*10*). Each subject was positioned head first, supine in the tomograph. The subject position was maintained for the duration of the acquisition using a thermoplastic mask for the head and 2 additional restraining straps wrapped around the subject's chest and lower abdomen and about the scanner bed to minimize arm and body movement between the CT and PET acquisitions as well as during the PET acquisition. A CT scout view was acquired to determine the CT and PET axial scan length. The acquisition field of view was defined from the scout view image to include the top of the head to mid thigh, resulting in 7 or 8 bed positions per whole-body scan depending on the height of the subject. Having defined the acquisition field of view, a minimal-dose CT scan was acquired, with an estimated total effective dose of 4.5 mSv. This CT dose estimate was calculated using the ImPACT CT Dosimetry Patient Calculator (http://www.impactscan.org/ctdosimetry.htm), with the following parameters: voltage, 140 kV; scan region, body; scan range, 1,015 mm; tube current, 60 mA; rotation time, 0.5 s; spiral pitch, 1.25; effective mAs, 24; and collimation, $16 \times 0.75 = 12$ mm. The CT images were converted from Hounsfield units to a 511-keV μ-map image, using segmentation and scaling, which was then forward-projected to create the attenuation correction for the PET emission data.

A dynamic acquisition consisting of 9 whole-body scans was acquired in 3-dimensional sinogram mode (span, 11; ring difference, 27). Emission data were acquired for 15 s/bed position for scans 1 and 2, 30 s/bed position for scans 3 and 4, 60 s/bed position for scans 5 and 6, 120 s/bed position for scan 7, 180 s/bed position for scan 8, and 240 s/bed position for scan 9. The total acquisition duration was dependent on the number of bed positions per whole-body acquisition and was 87.5 min for a 7-bed-position scan and 100 min for an 8-bed-position scan. These acquisition durations do not include the time required to move the bed between either successive bed positions or whole-body acquisitions. ^{11}C-CURB was injected by hand as a smooth bolus, followed by a 20-mL saline flush via an intravenous catheter in the antecubital fossa. The injection was started 15 s before the start of acquisition. The 15-s delay accounted for the circulation of the injectate through the body before arrival in the brain, at approximately the start of acquisition—that is, the first bed position. On completion of each whole-body acquisition, the bed was returned to the first bed position, and the next whole-body acquisition was started.

After acquisition, the data were transferred to an off-line workstation for reconstruction of the whole-body images. The data for each 3-dimensional whole-body sinogram were normalized and corrected

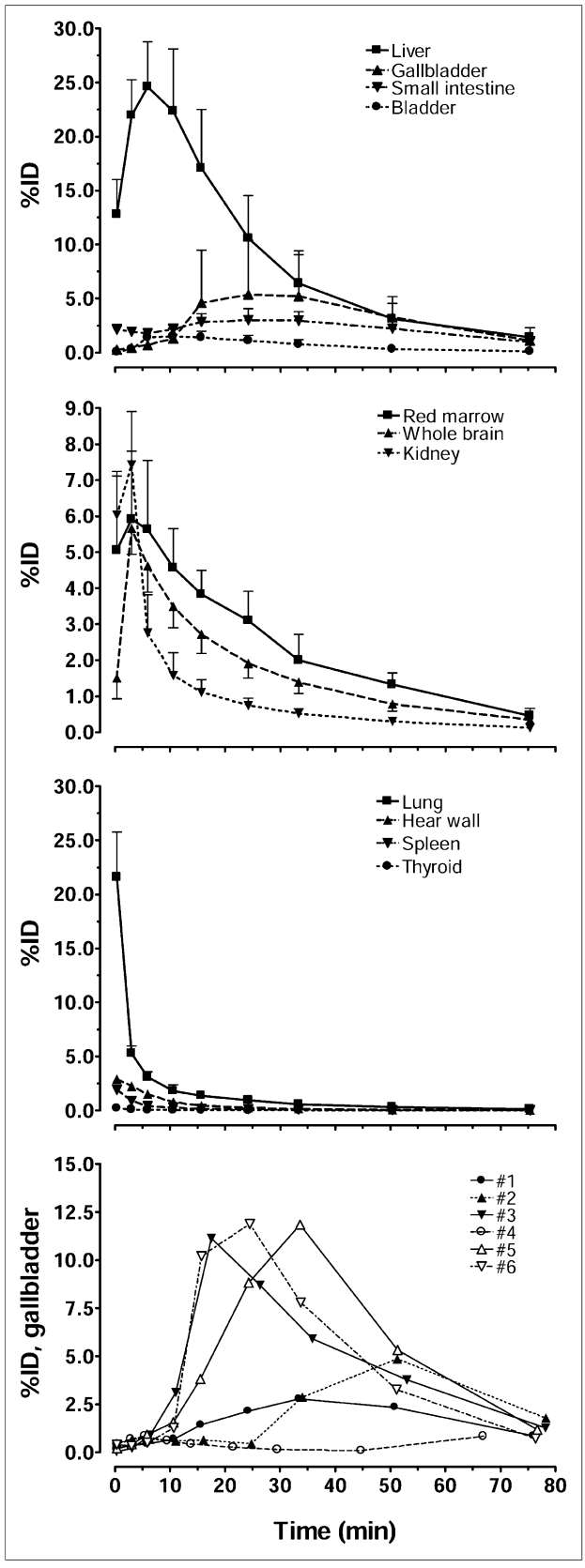

FIGURE 1. Mean organ uptake (expressed as %ID) for all 6 subjects over time. Vertical bars represent SD, and data are not decay-corrected to time 0. Differences existed among subjects in gallbladder uptake (bottom-most panel: solid symbols = men; open symbols = women).

TABLE 1
NCA Measured Assuming Organ Volume for Standard Man and Woman

Organ	All subjects (n = 6)*	Women only (n = 3)
Liver	0.117 ± 0.039	0.097 ± 0.042
Gallbladder	0.046 ± 0.026	0.040 ± 0.029
Small intestine	0.033 ± 0.008	0.030 ± 0.007
Red marrow	0.032 ± 0.006	0.028 ± 0.004
Whole brain	0.023 ± 0.003	0.022 ± 0.003
Lung	0.018 ± 0.003	0.014 ± 0.003
Kidney	0.013 ± 0.003	0.013 ± 0.002
Urinary bladder	0.009 ± 0.004	0.007 ± 0.003
Heart wall	0.005 ± 0.001	0.0040 ± 0.0003
Spleen	0.0020 ± 0.0004	0.0020 ± 0.0001
Thyroid	0.0004 ± 0.0001	0.00040 ± 0.00003

*Assuming standard male mass and density of organs of 6 subjects regardless of sex.

Data are mean ± SD in $MBq_{Organ}h/MBq_{Injected}$.

for attenuation and scatter before Fourier rebinning to convert the 3-dimensional sinograms into 2-dimensional sinograms (*11*). The 2-dimensional sinograms were reconstructed into image space twice: first, using an ordered-subset expectation maximization algorithm (*12*) with 4 iterations and 8 subsets, and second, using a direct inverse Fourier transform algorithm (*13*). After reconstruction, a gaussian filter of 5 mm in full width at half maximum in the 3 orthogonal planes was applied to the image. The images were calibrated to MBq/mL using a calibration factor determined before the acquisition. When all the bed positions had been reconstructed, including a correction for decay to the first bed position, a single whole-body image was constructed for each dynamic frame. Each reconstructed image had voxel dimensions of 2.7 × 2.7 × 2.0 mm (x,y,z) and transverse plane dimensions of 256 × 256 voxels (x,y). The number of planes (z) in the whole-body image is dependent on the number of bed positions acquired and was 429 or 487 planes for a 7- or 8-bed-position acquisition, respectively. The ordered-subset expectation maximization images were used for region-of-interest (ROI) placement because of the superior noise properties of iterative reconstructions, particularly in the chest and abdomen region, whereas the direct inverse Fourier transform images were used for dose assessment calculation because of the quantitative accuracy.

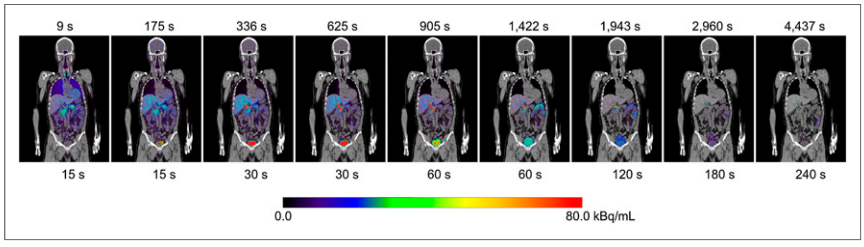

FIGURE 2. ^{11}C-CURB whole-body biodistribution over time for typical subject. PET (color scale) images are coregistered with subjects' CT image (gray scale). Times above each image are acquisition start times after injection of first bed position of whole-body image, and times below each image are duration of each bed position in whole-body image. Image sequence is not decay-corrected to injection time; decay correction is applied only when each whole-body image is created from its individual bed-position images.

Normalized Cumulated Activities (NCAs; i.e., Residence Times) and Absorbed Dose

The ROIs were defined using Analyze (Biomedial Imaging Resource). The selected ROIs (a total of 11, Fig. 1; Table 1) were whole brain, lung, kidney, liver, heart wall, small intestine, gallbladder, spleen, urinary bladder, thyroid, and red marrow (in the lumbar vertebrae), the organs displaying an activity concentration above background. The regions were described on the ordered-subset expectation maximization reconstructions to include the whole organ and on 6–10 adjacent planes. To avoid resolution-related spillover effect from adjacent regions (i.e., cross contamination from partial-volume effect) and apparent loss of count (if adjacent signal is low), ROIs were drawn well within the boundaries of the organ. The defined ROIs were then copied to the dynamic direct inverse Fourier transform whole-body series, and time–activity curves were extracted for each of the organs. The time–activity curves were converted from MBq/mL to MBq/organ using the organ mass and density for the reference adult man or woman (*14*), and NCA was calculated for each organ using trapezoidal integration of the area under the time–activity curves. It was assumed that after the end of acquisition, the dominant process was physical isotope decay of the injected ligand in the extrapolation of the time–activity curve to infinity. A remainder fraction was calculated by subtracting the individual organ NCA from the whole-body accumulated activity, which for ^{11}C is 0.490 h. For each subject, the NCA of each organ and the remainder were used in OLINDA/EXM 1.1 (*15*) to calculate the effective dose (using weighting factors as defined in International Commission on Radiological Protection publication 60 (*16*)) and the effective dose equivalent (using weighting factors as defined in International Commission on Radiological Protection publication 30 (*17*)) for the reference adult man (i.e., all the subjects, both men and women, have been modeled as a hermaphroditic adult standard man within OLINDA/EXM 1.1) and separately, for female values calculated assuming the reference adult female organ densities and volumes. The voiding bladder model was not assumed during the dose calculation in OLINDA/EXM 1.1.

RESULTS

^{11}C-CURB injected dose and specific activity were 345 ± 23 MBq and 60 ± 24 GBq/μmol, respectively, and mass injected was 2.1 ± 0.9 μg (ranging from 1.1 to 3.7 μg). ^{11}C-CURB injection did not result in any adverse reaction or observable effects as per subject self-report and physical/medical examinations before and after the scan. In addition, there were no clinically significant effects on vital measurements monitored during the study and on the following day's examination, including blood pressure, pulse, respiration rate, body temperature, electrocardiogram, and blood/urine tests.

Figure 2 depicts the dynamic biodistribution of ^{11}C-CURB during the 9-time-frame acquisition, and Figure 1 shows the extracted time–activity curves for the 11 organs with above-background uptake. Subjects had similar distribution of radioactivity for all the organs with the exception of that in the gallbladder, which showed much individual variability among subjects (Fig. 1, bottom-most panel). One subject (subject 4, a 30-y-old woman, Caucasian) had a peak uptake in the gallbladder of 0.8 percentage injected dose (%ID) at 5 min after injection, which was considerably lower than that in other subjects.

After injection, the greatest uptake was noted in the liver (Fig. 1), with a peak of 24.6 ± 4.2 %ID occurring during the third

TABLE 2
Organ Dose as Calculated by OLINDA/EXM 1.1

Organ	All subjects (SAHMM, $n = 6$) (μGy/MBq)*	Women only (SAFM, $n = 3$) (μGy/MBq)
Adrenals	3.60 ± 0.23	4.42 ± 0.32
Brain	5.46 ± 0.75	6.25 ± 0.84
Breasts	1.52 ± 0.21	2.08 ± 0.24
Gallbladder wall	111.2 ± 60.0	108.3 ± 75.4
Lower large intestine wall	2.28 ± 0.35	3.12 ± 0.49
Small intestine	12.15 ± 2.21	13.43 ± 2.31
Stomach wall	2.54 ± 0.11	3.40 ± 0.14
Upper large intestine wall	4.18 ± 0.28	5.06 ± 0.21
Heart wall	5.91 ± 0.45	5.98 ± 0.21
Kidneys	14.10 ± 2.86	14.57 ± 2.47
Liver	21.35 ± 6.63	23.50 ± 9.51
Lungs	5.80 ± 0.78	6.03 ± 0.93
Muscle	1.86 ± 0.20	2.50 ± 0.24
Ovaries	2.70 ± 0.34	3.54 ± 0.46
Pancreas	3.84 ± 0.36	4.61 ± 0.50
Red marrow	5.17 ± 0.63	4.96 ± 0.50
Osteogenic cells	4.23 ± 0.53	5.65 ± 0.76
Skin	1.30 ± 0.22	1.84 ± 0.26
Spleen	4.70 ± 0.60	5.69 ± 0.27
Testes	1.34 ± 0.33	—
Thymus	1.73 ± 0.29	2.42 ± 0.34
Thyroid	5.37 ± 0.85	6.27 ± 0.51
Urinary bladder wall	7.81 ± 2.86	8.14 ± 2.45
Uterus	2.71 ± 0.31	3.46 ± 0.42
Total body	2.81 ± 0.05	3.52 ± 0.07
Effective dose equivalent (μSv/MBq)	12.5 ± 3.8	13.0 ± 4.6
Effective dose (μSv/MBq)	4.6 ± 0.3	5.2 ± 0.3

*Assuming standard male mass and density of organs of 6 subjects regardless of sex.

SAHMM = standard adult hermaphrodite male model; SAFM = standard adult female model.

frame. At the end of acquisition, the liver had 1.4 ± 0.9 %ID, the maximum of all the organs. The lung, heart wall, spleen, and thyroid had monotonically decreasing radioactivity that peaked in the first frame and was quickly cleared. Activities in the brain, spinal red marrow, and kidney peaked in the second frame (3 min after injection); but the clearance was rapid in the kidney whereas the brain and red marrow showed slower and steady clearance. The urinary bladder, small intestine, and gallbladder wall had the late peaks of radioactivity in frames 3–5, 5–8, and 5–8, respectively, that were variable among subjects, indicating accumulation of excreted radiotracer or its metabolites and also the release from gallbladder into the small intestine.

Table 1 shows the normalized number of disintegrations for various organs. The first column shows the values calculated assuming standard male mass and density of the organs of the 6 subjects regardless of sex, and the second takes into account only the 3 female subjects and assumes standard mass for female organs. Table 2 shows the estimated radiation doses per organ calculated with OLINDA/EXM 1.1. The effective dose was 4.6 ± 0.3 μSv/MBq using the standard adult hermaphrodite male model and increased to 5.2 ± 0.3 μSv/MBq when only women were considered and the standard female model used. The largest absorbed dose (in μGy/MBq) was in the gallbladder (111 ± 60, ranging from 23 to 173), followed by the liver (21 ± 7), kidney (14 ± 3), and small intestine (12 ± 2).

DISCUSSION

We used a PET/CT scanner to measure the human temporal biodistribution of ^{11}C-CURB radioactivity concentration and to estimate radiation dose exposure to organs with the irreversible suicide radiotracer. PET/CT was sensitive enough to effectively acquire the organ and tissue concentration data for dosimetry calculations. We found that the effective dose of 4.6 ± 0.3 μSv/MBq for a standard adult hermaphrodite male model calculated with OLINDA/EXM 1.1 was within range of what has been previously reported from rat studies (4.4 μSv/MBq) and similar to other ^{11}C-labeled radioligands. A typical bolus injection of 370 MBq of ^{11}C-CURB should therefore lead to an effective dose around 1.7 mSv, and the most affected organ would be the gallbladder wall (111 ± 60 μGy/MBq). The high dose of radiation in the gallbladder, compared with other tracers, can be attributed to a higher hepatobiliary clearance (Fig. 1) and the rapid metabolism of *O*-arylcarbamates compounds (i.e., CURB/URB694) where half of the parent compound is metabolized in the first 20 m after injection (*8*). The gallbladder time–activity curve is not uniformly reported in other dosimetry papers but is not unique to ^{11}C-CURB (*18,19*). The large variance in gallbladder uptake of radioactivity observed is attributed to variable hepatobiliary clearance and gallbladder emptying among the subjects. The gallbladder effective dose (41 mSv for a typical injection of 370 MBq) is below common regulatory limits. For example, the U.S. Food and Drug Administration establishes 30 mSv for a single study and 50 mSv annually for the whole body for active blood-forming organs, lens of the eye, and gonads and 50 mSv for a single study and 150 mSv annually for other organs (*20*).

We investigated sex differences in dosimetry. When the female adult phantom was used, women ($n = 3$) had a 13% higher effective dose relative to the value obtained when the full set of subjects was used with the hermaphrodite male model. Although we note that when human dosimetry is calculated, data should be investigated separately for the sexes, the present finding, in a small number of subjects suggests that both men and women can safely take part in an equal number of scans each year.

For our study, when the whole-body PET/CT Biograph HiRez XVI was used, the effective dose of the minimal-dose CT scan for the whole-body adult man was estimated to be 4.5 mSv, a dose significantly higher than that from ^{11}C-CURB. However, the effective doses of a CT scan used to provide attenuation data for a neurologic PET scan can be reduced to 0.07 mSv (also estimated using the ImPACT CT Dosimetry Patient Calculator with the following parameters: voltage, 60 kV; scan region, brain; rotation time, 0.5 s; spiral pitch, 1.25; effective mAs, 23; and collimation, 16 × 0.75 = 12 mm), which

is markedly lower than that of a typical diagnostic neurologic CT scan (~2.5 mSv).

Several assumptions have been made to allow for an estimation of the effective dose of ^{11}C-CURB. First, we assumed that in the interleaved planes of the whole-body images, the kinetics of the ligand were the same and that the main effect was decay. Although this was obviously not the case during the early phases of ligand delivery, the effect was minimized when small acquisition durations were chosen for this part of the scan. An attempt was made during the definition of the acquisition length to position the center of the larger organs, such as the liver, brain, and heart, at or toward the center of a single bed position. Alternatively, the ROI could be described on the individual bed-position images, thereby avoiding this effect. Second, we assumed that the volume of the bladder was constant for the duration of the acquisition, which was clearly not the case because radioactivity present in the bladder grew in volume over the course of the acquisition as the ligand was excreted from the blood into the urine. A better solution would be to describe a volume ROI that increases as the bladder grows over the duration of the acquisition, with the smallest volume for the early time frames. However, for the sake of consistency with previously reported dosimetry studies, this method was not used.

CONCLUSION

The ^{11}C-CURB effective dose in an adult human was estimated to be 4.6 ± 0.3 μSv/MBq, or 1.7 mSv for a typical injection of 370 MBq, and was slightly higher in women. The gallbladder was the organ receiving the highest dose exposure of 111 μGy/MBq, which was equivalent to 41 mSv for a typical injection of 370 MBq of ^{11}C-CURB and was below the Food and Drug Administration single-scan dose limit for that organ. These dose estimates would allow 2 repeated scans within a calendar year in the same subject and remain within regulatory guidelines.

DISCLOSURE

The costs of publication of this article were defrayed in part by the payment of page charges. Therefore, and solely to indicate this fact, this article is hereby marked "advertisement" in accordance with 18 USC section 1734. This study was supported by Canada Foundation for Innovation and the Ontario Ministry of Research and Innovation. No other potential conflict of interest relevant to this article was reported.

ACKNOWLEDGMENTS

We thank Armando Garcia, Winston Stableford, and Min Wong for their excellent technical assistance.

REFERENCES

1. Cravatt BF, Giang DK, Mayfield SP, Boger DL, Lerner RA, Gilula NB. Molecular characterization of an enzyme that degrades neuromodulatory fatty-acid amides. *Nature.* 1996;384:83–87.
2. Thomas EA, Cravatt BF, Danielson PE, Gilula NB, Sutcliffe JG. Fatty acid amide hydrolase, the degradative enzyme for anandamide and oleamide, has selective distribution in neurons within the rat central nervous system. *J Neurosci Res.* 1997;50:1047–1052.
3. Mulder J, Aguado T, Keimpema E, et al. Endocannabinoid signaling controls pyramidal cell specification and long-range axon patterning. *Proc Natl Acad Sci USA.* 2008;105:8760–8765.
4. Egertová M, Giang DK, Cravatt BF, Elphick MR. A new perspective on cannabinoid signalling: complementary localization of fatty acid amide hydrolase and the CB1 receptor in rat brain. *Proc Biol Sci.* 1998;265:2081–2085.
5. Clapham DE, Julius D, Montell C, Schultz G. International union of pharmacology. XLIX. nomenclature and structure-function relationships of transient receptor potential channels. *Pharmacol Rev.* 2005;57:427–450.
6. McKinney MK, Cravatt BF. Structure and function of fatty acid amide hydrolase. *Annu Rev Biochem.* 2005;74:411–432.
7. Wilson AA, Garcia A, Parkes J, Houle S, Tong J, Vasdev N. ^{11}C- CURB: evaluation of a novel radiotracer for imaging fatty acid amide hydrolase by positron emission tomography. *Nucl Med Biol.* 2011;38:247–253.
8. Rusjan PM, Wilson AA, Mizrahi R, et al. Mapping human brain fatty acid amide hydrolase activity with PET. *J Cereb Blood Flow Metab.* 2013;33:407–414.
9. Spitzer RL, Williams JBW, Gibbon M, First MB. The structured clinical interview for DSM-III-R, I: history, rationale and description. *Arch Gen Psychiatry.* 1992;49:624–629.
10. Brambilla M, Secco C, Dominietto M, Matheoud R, Sacchetti G, Inglese E. Performance characteristics obtained for a new 3-dimensional lutetium oxyorthosilicate-based whole-body PET/CT scanner with the National Electrical Manufacturers Association NU 2-2001 standard. *J Nucl Med.* 2005;46:2083–2091.
11. Defrise M, Kinahan PE, Townsend DW, Michel C, Sibomana M, Newport D. Exact and approximate rebinning algorithms for 3-D PET data. *IEEE Trans Med Imaging.* 1997;16:145–158.
12. Hudson HM, Larkin RS. Accelerated image reconstruction using ordered subsets of projection data. *IEEE Trans Med Imaging.* 1994;13:601–609.
13. Hamill JJ, Hawman EG. Evaluating a frequency-space SPECT reconstruction algorithm. *Proc SPIE 2622.* 1995;2622:785–791.
14. Valentin J. Basic anatomical and physiological data for use in radiological protection: reference values—ICRP publication 89. *Ann ICRP.* 2002;32:5–265.
15. Stabin MG, Sparks RB, Crowe E. OLINDA/EXM: the second-generation personal computer software for internal dose assessment in nuclear medicine. *J Nucl Med.* 2005;46:1023–1027.
16. International Commission on Radiological Protection (ICRP). 1990 Recommendations of the International Commission on Radiological Protection. ICRP publication 60. *Ann ICRP.* 1991;21(1–3).
17. International Commission on Radiological Protection (ICRP). Limits for intakes of radionuclides by workers: an addendum. ICRP publication 30 (part 4). *Ann ICRP.* 1988;19(4).
18. Wong DF, Waterhouse R, Kuwabara H, et al. ^{18}F-FPEB, a PET radiopharmaceutical for quantifying metabotropic glutamate 5 receptors: a first-in-human study of radiochemical safety, biokinetics, and radiation dosimetry. *J Nucl Med.* 2013;54:388–396.
19. Challapalli A, Kenny LM, Hallett WA, et al. ^{18}F-ICMT-11, a caspase-3-specific PET tracer for apoptosis: biodistribution and radiation dosimetry. *J Nucl Med.* 2013;54:1551–1556.
20. Title 21: Food and drugs—radioactive drugs for certain research uses. 21 Code of Federal Regulations 361.1. U.S. Food and Drug Administration website. http://www.accessdata.fda.gov/scripts/cdrh/cfdocs/cfcfr/CFRSearch.cfm?FR=361.1. Accessed October 28, 2014.